# Quantum phase transition between spin liquid and spin nematics in spin-1 Kitaev honeycomb model

Tohru Mashiko* and Tsuyoshi Okubo†
*Department of Physics, The University of Tokyo, Tokyo 113-0033, Japan*

(Received 8 April 2024; accepted 8 July 2024; published 26 July 2024)

Besides the exactly solvable spin-1/2 Kitaev model, higher spin-$S$ ones, not exactly solvable, are promising playgrounds for researches on the quantum spin liquid as well. One of the main interests in higher spin-$S$ cases is the interplay between the Kitaev spin liquid (KSL) and spin nematics. We probe this interplay in a spin-1 model on the honeycomb lattice with competing bilinear-biquadratic and Kitaev interactions. Utilizing the 2D infinite projected entangled-pair state (iPEPS), we map out the phase diagram for the ferro-biquadratic interaction. In the phase diagram, we discover the direct phase transitions between the KSL phases and ferro-quadrupolar ordered spin nematic phase, which we call the FQ phase. It has been revealed that the ferro KSL exhibits robustness against perturbations from ferro-quadrupolar interactions. Also, the FQ phase is extended to the parameter region near the antiferro-Kitaev limit.

DOI: 10.1103/PhysRevResearch.6.033110

## I. INTRODUCTION

The exactly solvable spin-1/2 Kitaev honeycomb model (KHM) exhibits [1] quantum spin liquids as the ground state, called the Kitaev spin liquid (KSL), ascribed for the bond-dependent spin-spin interactions giving rise to the frustration. This KHM possesses the $\mathbb{Z}_2$ gauge structure of the Majorana fermions, i.e., the conservation of the flux, on each local hexagonal plaquette. The Kitaev interactions can be realized in materials with strong spin-orbit couplings (SOCs) [2]. There appeared a number of successive experiments with candidate Kitaev materials {e.g., $\alpha$-$RuCl_3$ [3–9], $A_2IrO_3$ ($A$ = Na, Li) [10–18] and $H_3LiIr_2O_6$ [19]}, which then motivated researchers for more theoretical investigations [20–27].

Besides the spin-1/2 KHM, higher spin-$S$ ones have also attracted attentions, despite the difficulties because of the absence of exact solutions. Analytical studies of arbitrary spin-$S$ Kitaev models have confirmed [28] the conservation of $\mathbb{Z}_2$ gauge flux, similar to the case of spin-1/2, and the disappearance of spin-spin correlations beyond nearest neighbors. Several numerical studies supported the existence of quantum spin liquids in spin-1 KHMs [29–34]. Candidate materials were also proposed in spin-1 [35] and spin-3/2 [36,37] cases.

Higher internal degrees of freedom than spin-1/2 cause unique spin-quadrupolar (or multipolar) states. One of the most representative ones is the spin nematic state characterized by the spin-quadrupolar order. The interplay between the quantum spin liquid and spin nematic state has been regarded as a significant topic, which cannot be observed in the classical system but in the quantum system. One may discover novel quantum properties of matters by investigating this interplay on the KHM whose ground state is verified to be the quantum spin liquid. However, this is far from understood since it is hard to investigate their "hidden" magnetism. Namely, both states do not exhibit the long-range spin-dipolar order, although they are different in that the spin nematic state breaks spin rotational symmetry owing to the order of the spin-quadrupolar moments [38–42] while quantum spin liquids including the KSL do not spontaneously break any symmetries [43].

Recently, Pohle *et al.* addressed [44,45] this challenging problem by investigating a spin-1 honeycomb model with competing bilinear-biquadratic (BBQ) and Kitaev interactions, which we call the BBQ-K model defined as

$$\hat{H}_{\mathrm{BBQ-K}} \equiv \sum_{\gamma=x,y,z} \sum_{\langle i,j\rangle_\gamma} \hat{H}^{\langle i,j\rangle_\gamma}_{\mathrm{BBQ-K}}, \tag{1}$$

$$\hat{H}^{\langle i,j\rangle_\gamma}_{\mathrm{BBQ-K}} \equiv J_1 \hat{\mathbf{S}}_i \cdot \hat{\mathbf{S}}_j + J_2 \left(\hat{\mathbf{S}}_i \cdot \hat{\mathbf{S}}_j\right)^2 + K \hat{S}^\gamma_i \hat{S}^\gamma_j . \tag{2}$$

Here, $\langle i, j\rangle_\gamma$ denotes the nearest-neighbor pair on a $\gamma$ bond. $J_1$, $J_2$, and $K$ are coupling coefficients of Heisenberg (bilinear), biquadratic, and Kitaev terms respectively. They discovered a variety of quantum properties caused by the competition between these interactions. However, several properties including phases and phase transitions are still unclear when the Kitaev interaction prevail over the BBQ ones. This is because it is in principle impossible for semiclassical variational calculations adopted in Refs. [44,45] to illustrate quantum spin liquid.

In this paper, we investigate the BBQ-K model to explore quantum phases and phase transitions, extended to the parameter regions where the Kitaev interaction is dominant. We here adopted the tensor network method, that is the 2D infinite projected entangled-pair state (iPEPS) [46–48], to accurately

*Contact author: t-mashiko@phys.s.u-tokyo.ac.jp
†Contact author: t-okubo@phys.s.u-tokyo.ac.jp

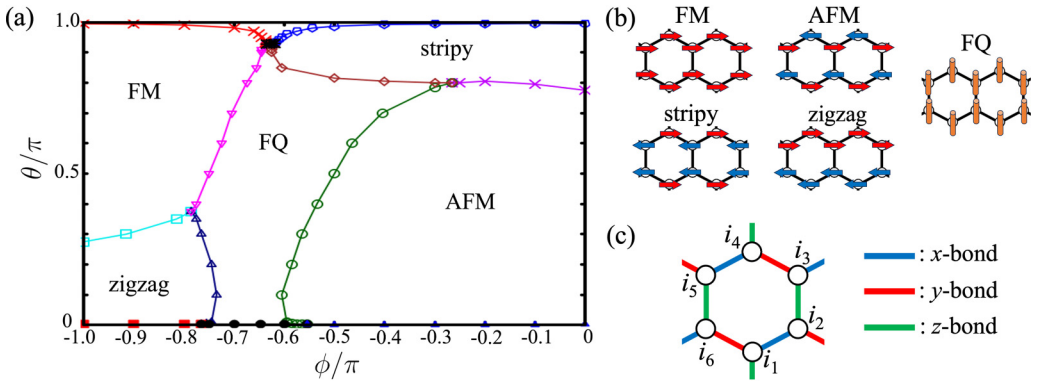


FIG. 1. (a) Phase diagram of the BBQ-K model in the region of $0.0 \leqslant \theta/\pi \leqslant 1.0$ and $-1.0 \leqslant \phi/\pi \leqslant 0.0$. (b) Configurations of antiferromagnetic (AFM), ferromagnetic (FM), stripy, zigzag, and ferro-quadrupolar ordered spin nematic (FQ) phases. The arrows and rods denote spin dipolar and quadrupolar moments, respectively. (c) Hexagonal plaquette with sites $\{i_1, i_2, \cdots, i_6\}$. The blue, red, and green lines denote bonds of local tensors along $x$, $y$, and $z$ directions of the Kitaev term respectively.

capture the quantum entanglements among spins, which was neglected in Refs. [44,45].

As a result, we obtain the phase diagram Fig. 1(a). Following the notation in Refs. [44,45], we normalize the coefficients in Eq. (2) with two parameters $\theta$ and $\phi$ as $(J_1, J_2, K) \equiv (\sin\theta\cos\phi, \sin\theta\sin\phi, \cos\theta)$. Similar to Refs. [44,45], Fig. 1(a) depicts four spin-dipolar ordered phases: antiferromagnetic (AFM), ferromagnetic (FM), zigzag, stripy phases, and the ferro-quadrupolar ordered spin nematic phase, which we call the FQ phase later [see Fig. 1(b)]. However, unlike Refs. [44,45], strong competition between the Kitaev and ferro-biquadratic (ferro-quadrupolar) terms causes unconventional quantum properties: (1) two extended KSL phases and (2) the direct KSL–FQ transitions. We describe details of these results in Sec. IV. We focus on only the parameter region of the negative quadrupolar interaction $J_2 < 0$ ($-\pi \leqslant \phi \leqslant 0$). This is because, in the other region $J_2 > 0$ ($0 \leqslant \phi \leqslant \pi$), there are several disagreements between previous researches [44,45,49] as for the ground-state phases, and there are a number of candidate phases in close energy scales. Therefore, distinguishing a phase from the other candidates requires more computational costs and larger-scale calculations.

This paper is organized as follows. In Sec. II, we describe the BBQ-K model. Then, we show the details of the tensor network method in Sec. III. We present our numerical results: detailed phase diagrams and how to detect phases and boundaries, in Sec. IV. Then we discuss the nature of BBQ-K model in Sec. V, including implications for experiments to capture the phase diagram.

## II. BBQ-K MODEL

In this section, we describe the BBQ-K model Eqs. (1) and (2) in more detail. At the limit of $\theta = 0$ ($\pi$) [$J_1 = J_2 = 0$ and $K = 1$ ($-1$)], Eq. (1) is nothing but the spin-1 Kitaev model whose ground state is antiferro- (ferro-) KSL, which we call the AKSL (FKSL). These Hamiltonians commute [28] with the $\mathbb{Z}_2$ gauge flux operator $\hat{W}_p$ on a hexagonal plaquette with sites $\{i_1, i_2, \cdots, i_6\}$ shown in Fig. 1(c), defined as

$$\hat{W}_p \equiv \hat{U}^z_{i_1}\hat{U}^y_{i_2}\hat{U}^x_{i_3}\hat{U}^z_{i_4}\hat{U}^y_{i_5}\hat{U}^x_{i_6}, \tag{3}$$

where $\hat{U}^\gamma_i \equiv \exp(i\pi\hat{S}^\gamma_i)$ and $\gamma = x, y, z$. These spin-1 KSL states are characterized by the vortex freeness, i.e., $\langle\hat{W}_p\rangle = +1$, according to a study of the spin-wave theory [28] and numerical studies [30,31].

The limit of $\theta = \pi/2$ ($K = 0$) is the BBQ model. The biquadratic term $(\hat{\boldsymbol{S}}_i \cdot \hat{\boldsymbol{S}}_j)^2$ can be decomposed with the spin-quadrupolar operator $\hat{\boldsymbol{Q}}_i$ at site $i$, as

$$(\hat{\boldsymbol{S}}_i \cdot \hat{\boldsymbol{S}}_j)^2 = \tfrac{1}{2}(\hat{\boldsymbol{Q}}_i \cdot \hat{\boldsymbol{Q}}_j - \hat{\boldsymbol{S}}_i \cdot \hat{\boldsymbol{S}}_j) + \tfrac{4}{3}, \tag{4}$$

where the term $\hat{\boldsymbol{Q}}_i \cdot \hat{\boldsymbol{Q}}_j$ stabilizes the spin nematic ground state. $\hat{\boldsymbol{Q}}_i$ has five components: $(\hat{S}^x_i)^2 - (\hat{S}^y_i)^2$, $\sqrt{3}[(\hat{S}^z_i)^2 - (2/3)]$, $\hat{S}^x_i\hat{S}^y_i + \hat{S}^y_i\hat{S}^x_i$, $\hat{S}^y_i\hat{S}^z_i + \hat{S}^z_i\hat{S}^y_i$, and $\hat{S}^z_i\hat{S}^x_i + \hat{S}^x_i\hat{S}^z_i$. If $J_2 < 0$, the FQ phase is stabilized [49]. If $J_2 > 0$, the antiferro-quadrupolar (AFQ) ordered phase appears in the classical case [50,51], whereas this quadrupolar order is melted [49,52] by quantum fluctuations.

## III. TENSOR NETWORK METHOD

In our numerical calculations, we implemented variational calculations by the iPEPS [46–48]. Here, we provide an overview of the algorithms.

In the case of the finite-size system, the ground state $|\Psi\rangle$ of a spin-1 system with $N$ sites can be expressed by direct products of local spin-1 states as

$$|\Psi\rangle \equiv \sum_{\{s_i=0,\pm1\}} \Psi^{s_0\cdots s_{N-1}}|s_0\rangle \otimes \cdots \otimes |s_{N-1}\rangle, \tag{5}$$

where $s_i = 0, \pm1$ denotes the quantum number of $\hat{S}^z_i$. We approximate the ground-state wave function $\Psi^{s_0\cdots s_{N-1}}$ as a project entangled-pair state (PEPS) [53,54] with $N$ local tensors $\psi^{s_i}_{l_i m_i n_i}$ as

$$\Psi^{s_0\cdots s_{N-1}} \approx \mathrm{Tr}\left(\prod_{i=0}^{N-1}\psi^{s_i}_{l_i m_i n_i}\right), \tag{6}$$

where Tr stands for the contraction of all virtual indices $\{l_i m_i n_i\}$, which correspond to edges of the honeycomb lattice. We define the bond dimension of virtual indices as $D$. We consider the iPEPS by enforcing translational symmetry in the PEPS to calculate physical quantities in the thermodynamic

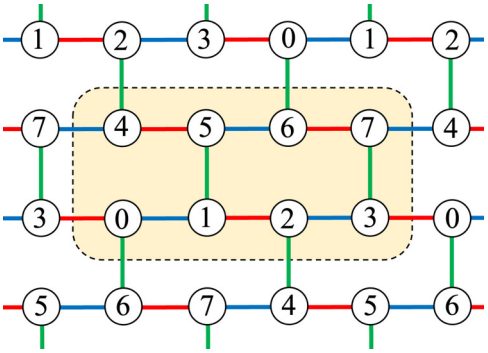


FIG. 2. Eight sublattices in a unit cell with periodic boundary conditions. The blue, red, and green lines denote bonds of local tensors along $x$, $y$, and $z$ directions of the Kitaev term, respectively.

limit. We assume N-sublattice structure in a unit cell. The iPEPS can express a larger space of quantum states for larger $D$ (arbitrary quantum states in the case of $D \to \infty$). Since we here consider only short-range interactions, we can assume that the entanglement entropy obeys the area law [55–57], which allows us to efficiently approximate the ground state even with the finite bond dimension $D$ [58].

Next, we search for the objective ground state $|\Psi\rangle$ making use of the imaginary-time evolution (ITE) as $|\Psi\rangle \simeq e^{-T\hat{H}}|\Psi_0\rangle$, where $T$ is a sufficiently long imaginary time and $|\Psi_0\rangle$ is an initial state. By the first-order Trotter-Suzuki decomposition [59–61], the ITE is split into a product of local two-body Hamiltonians $\hat{H}_{ij}$ ($\hat{H} = \sum_{\langle i,j\rangle} \hat{H}_{ij}$) with nearest-neighbor interactions

$$e^{-T\hat{H}}|\Psi_0\rangle = \left[\left(\prod_{\langle i,j\rangle} e^{-\tau \hat{H}_{ij}}\right)^{N_\tau} + O(\tau)\right]|\Psi_0\rangle, \qquad (7)$$

where $N_\tau = T/\tau$ is the number of ITE steps. We neglect $O(\tau)$ by setting $\tau$ as a sufficiently small value, and iterate the ITE steps until it converges. In practice, after multiplying $e^{-\tau \hat{H}_{ij}}$, we truncate the bond dimension by the simple update method [62,63], so that this remains $D$ throughout the ITE steps. Note that we should start the ITE steps from a variety of possible initial conditions so as to reduce the influence of being trapped in a local minimum.

We then derive the expectation value of a physical quantity $\hat{O}$ defined as $\langle\hat{O}\rangle \equiv \langle\Psi|\hat{O}|\Psi\rangle/\langle\Psi|\Psi\rangle$. By contracting indices $s_i$ in Eq. (6), $\langle\Psi|\hat{O}|\Psi\rangle$ and $\langle\Psi|\Psi\rangle$ can also be expressed as an infinite tensor network with the bond dimension $D^2$. We accurately approximated this as a finite one with the help of the corner transfer matrix renormalization group (CTMRG) method [64–69] for an arbitrary unit-cell structure [70]. The accuracy of the CTMRG is determined by the bond dimension $\chi$ of the corner matrices and the edge tensors. We choose $\chi$ as $\chi \propto D^2$.

In the present iPEPS simulations, we adopt the tensor network library TeNeS [71,72]. We define the iPEPS in a unit cell with eight sublattices (see Fig. 2). Each circle denotes a local tensor $\psi^{s_i}_{l_i m_i n_i}$ in Eq. (6). As for the ITE, we set $\tau = 10^{-2}$ and $N_\tau = 10^4$ so that the ITE well converges. Based on the results in Refs. [44,45], we prepare seven initial conditions for the ITE: AFM, FM, stripy, zigzag, and FQ states in addition to antiferro- and ferro-loop gas states (LGSs) [25,31], which qualitatively capture the nature of AKSL and FKSL states respectively. At a single parameter point $(\theta, \phi)$, we perform the ITE under these seven initial conditions. We then employ a state where the energy becomes the lowest. Considering the convergence of energy at Kitaev limits in Ref. [31], we set the bond dimensions as $(D, \chi) = (8, 64)$ or $(8, 128)$, described in the next section in more detail.

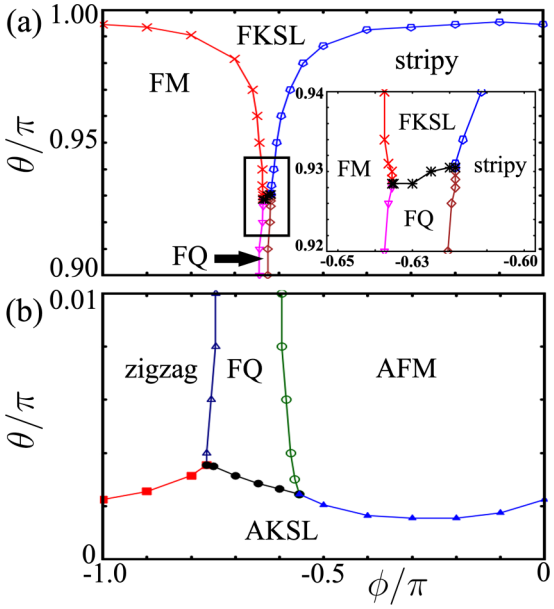


FIG. 3. Phase diagram of the BBQ-K model. (a) The vicinity of the ferro-Kitaev limit ($\theta = \pi$) with the inset closing up the black squared region, and (b) the vicinity of the antiferro-Kitaev limit ($\theta = 0$).

## IV. RESULTS

In this section, we give numerical results. Figure 3 shows the close-up of the phase diagram Fig. 1(a) in the vicinity of the Kitaev limits ($\theta = 0$ and $\pi$). We explain these phase diagrams in Sec. IV A. In Secs. IV B and IV C, we describe how to detect different phases and in the vicinity of ferro- and antiferro-Kitaev limits, respectively.

As for the bond dimensions of iPEPS, we adopt $(D, \chi) = (8, 128)$ in the black-squared region of Fig. 3(a) and when determining the AKSL–FQ boundaries in Fig. 3(b), so that the CTMRG well converges. In the other parameter regions, we adopt $(D, \chi) = (8, 64)$. Also, the results when we change the bond dimension $D$ are described in Appendix, where we confirm that $D = 8$ are sufficient to draw proper conclusions.

### A. Ground-state phase diagram

In Fig. 3, there are phase transitions between the KSL and the four spin-dipolar ordered phases. Considering the Kitaev–Heisenberg model ($\phi/\pi = -1.0$ or $0.0$), our results of boundaries between these phases are consistent with the density matrix renormalization group (DMRG) calculation [32]. More interestingly, we discover the direct KSL–FQ transitions

appear in the vicinity of both Kitaev limits. This result is significant since these transitions are in principle impossible to detect until one accurately capture quantum fluctuations and entanglements by iPEPS.

In the vicinity of the ferro-Kitaev limit ($\theta = \pi$), we confirm that the FKSL phase drastically gets extended around the region of $-0.65 \leqslant \phi/\pi \leqslant -0.6$ [see Fig. 3(a)]. In this region, the ferro-quadrupolar term of the BBQ model is dominant compared to the Heisenberg one. Especially at $\phi = \arctan(2)$ ($\approx -0.648\pi$), the BBQ-K model Eq. (2) can be rewritten without the the Heisenberg term as

$$\hat{H}_{\mathrm{BBQ-K}}^{\langle i,j\rangle_\gamma} = -\frac{\sin\theta}{\sqrt{5}}\left(\hat{\boldsymbol{Q}}_i \cdot \hat{\boldsymbol{Q}}_j + \frac{8}{3}\right) + \cos\theta \hat{S}_i^\gamma \hat{S}_j^\gamma. \quad (8)$$

We thus interpret it as meaning that the FKSL phase is robust against perturbations from ferro-quadrupolar interactions. Moreover, there is not the direct FM–stripy transition unlike Refs. [44,45] since KSL or FQ phase exists between FM and stripy phases. We find that this intermediate FQ phase appears since it is more robust against the Heisenberg interaction than one in Refs. [44,45], as iPEPS accurately capture quantum entanglements.

In the vicinity of the antiferro-Kitaev limit ($\theta = 0$) shown in Fig. 3(b), we also discover that the FQ phase is also more robust against the antiferro-Kitaev interaction than one in Refs. [44,45], while the AKSL phase is vulnerable to both Heisenberg and ferro-quadrupolar interactions. Note that the FQ phase gets extended when the antiferro-Kitaev interaction becomes dominant, which shrinks in Refs. [44,45]. Also, there is not the direct zigzag–AFM transition since the FQ phase gets between these two phases. We reveal quantum properties caused by the competition between antiferro-Kitaev and ferro-quadrupolar interactions by iPEPS.

### B. Vicinity of the ferro-Kitaev limit

In this subsection, we explain how to calculate order parameters for determining phases and boundaries with the emphasis on the vicinity of ferro-Kitaev limit ($\theta = \pi$). In later subsubsections, we show our numerical results in the cases of the FQ–FKSL and FM–FQ–stripy transitions.

#### *1. FQ–FKSL transition*

In this subsubsection, we show our numerical results illustrating the FQ–FKSL transition. We derive some order parameters to determine phases and the boundary when tuning the parameter $\theta$ and fixing $\phi$ at $\phi = -0.63\pi$.

Here, we calculate the norm of the spin dipolar moment to investigate magnetic orders [see Fig. 4(a)], defined as

$$|\langle\hat{\boldsymbol{S}}\rangle| \equiv \frac{1}{8}\sum_{i\in\{0,\cdots,7\}} \sqrt{\langle\hat{S}_i^x\rangle^2 + \langle\hat{S}_i^y\rangle^2 + \langle\hat{S}_i^z\rangle^2}. \quad (9)$$

In Eq. (9), $i \in \{0, \cdots, 7\}$ means the eight sublattices in the unit cell shown in Fig. 2. $|\langle\hat{\boldsymbol{S}}\rangle|$ takes a finite value if the system has any magnetic orders, and 0 otherwise. As shown in Fig. 4(a), $|\langle\hat{\boldsymbol{S}}\rangle|$ stays 0 in the whole range of $0.90 \leqslant \theta/\pi \leqslant 1.0$, which corresponds to characteristics of FQ and FKSL phases without spin-dipolar order.

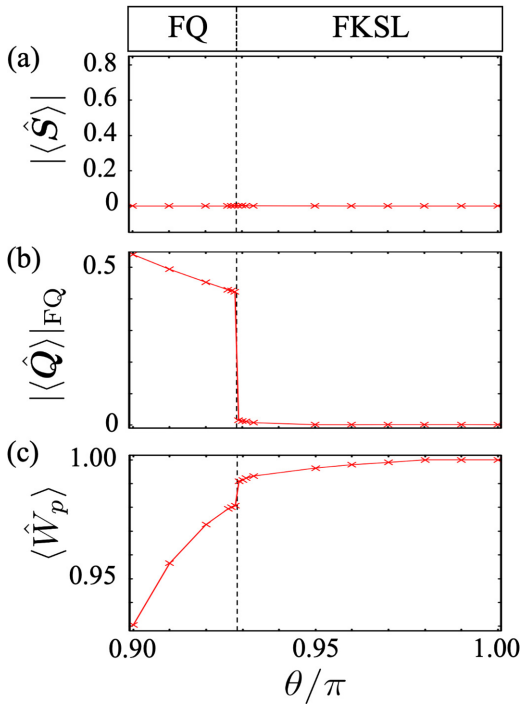


FIG. 4. Numerical results as a function of $\theta$ when fixing $\phi$ at $\phi = -0.63\pi$. (a) Norm of spin $|\langle\hat{\boldsymbol{S}}\rangle|$, (b) ferro-quadrupolar order parameter $|\langle\hat{\boldsymbol{Q}}\rangle|_{\mathrm{FQ}}$, (c) flux $\langle\hat{W}_p\rangle$. The dashed line is the phase boundary between FQ phase and FKSL phase, $\theta/\pi \approx 0.9285$. Here, we set $(D, \chi) = (8, 128)$.

Next, we investigate the ferro-order of the quadrupolar moment $|\langle\hat{\boldsymbol{Q}}\rangle|_{\mathrm{FQ}}$, defined as

$$|\langle\hat{\boldsymbol{Q}}\rangle|_{\mathrm{FQ}} \equiv \sqrt{\sum_{\gamma'=1}^{5}\left(\frac{1}{8}\sum_{i\in\{0,\cdots,7\}}\langle\hat{Q}_i^{\gamma'}\rangle\right)^2}. \quad (10)$$

$|\langle\hat{\boldsymbol{Q}}\rangle|_{\mathrm{FQ}}$ takes finite values in the case of ferro-quadrupolar ordered state, and 0 in the other cases. We confirm a sharp jump of $|\langle\hat{\boldsymbol{Q}}\rangle|_{\mathrm{FQ}}$ [see Fig. 4(b)] at $\theta/\pi \approx 0.9285$, and the left-hand side area $0.9 \leqslant \theta/\pi \lesssim 0.9285$ is the FQ phase. $|\langle\hat{\boldsymbol{Q}}\rangle|_{\mathrm{FQ}}$ becomes small but finite in the right-hand side area near the boundary $\theta/\pi \approx 0.9285$. However, we expect that this approaches to 0 if we increase the bond dimension $D$.

We examine the vortex freeness in this parameter region by calculating the expectation value of the flux $\hat{W}_p$ in Eq. (3), defined as $\langle\hat{W}_p\rangle \equiv \frac{1}{4}\sum_{j=1}^{4}\langle\hat{W}_{p_j}\rangle$. $\hat{W}_{p_j}$ means the flux on the plaquette $p_j$ in the Fig. 2, defined as

$$\hat{W}_{p_1} \equiv \hat{U}_0^z\hat{U}_1^y\hat{U}_5^x\hat{U}_4^z\hat{U}_7^y\hat{U}_3^x, \quad \hat{W}_{p_2} \equiv \hat{U}_2^z\hat{U}_3^y\hat{U}_7^x\hat{U}_6^z\hat{U}_5^y\hat{U}_1^x,$$
$$\hat{W}_{p_3} \equiv \hat{U}_5^z\hat{U}_6^y\hat{U}_0^x\hat{U}_3^z\hat{U}_2^y\hat{U}_4^x, \quad \hat{W}_{p_4} \equiv \hat{U}_7^z\hat{U}_4^y\hat{U}_2^x\hat{U}_1^z\hat{U}_0^y\hat{U}_6^x.$$

Figure. 4(c) shows a small jump of $\langle\hat{W}_p\rangle$ at the boundary $\theta/\pi = 0.9285$. In the right-hand side area $0.9285 \lesssim \theta/\pi \leqslant 1.0$, the FKSL phase is extended without any other intermediate phases since $|\langle\hat{\boldsymbol{S}}\rangle| = |\langle\hat{\boldsymbol{Q}}\rangle|_{\mathrm{FQ}} \approx 0$ and $\langle\hat{W}_p\rangle \approx 1$. Interestingly, $\langle\hat{W}_p\rangle$ takes the value near to 1 even in the FQ phase, which means that the FQ phase shows the vortex freeness strongly influenced by the FKSL phase.

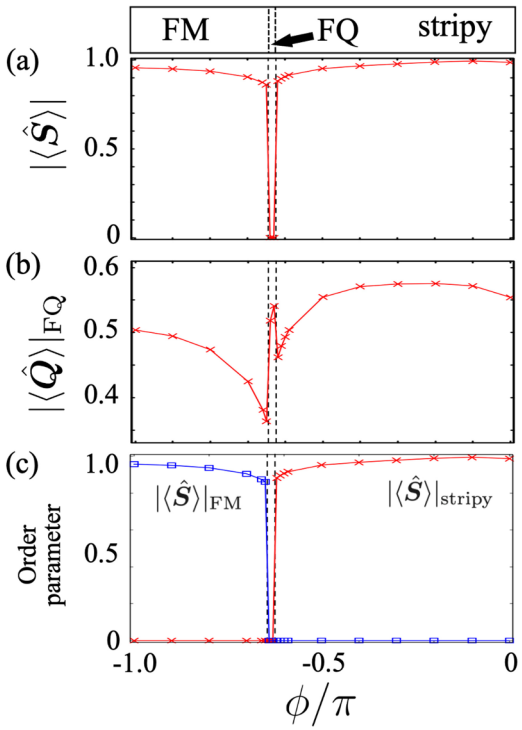


FIG. 5. Numerical results as a function of $\phi$ when fixing $\theta$ at $\theta = 0.9\pi$. (a) Norm of spin $|\langle\hat{\boldsymbol{S}}\rangle|$, (b) ferro-quadrupolar order parameter $|\langle\hat{\boldsymbol{Q}}\rangle|_{\rm FQ}$, (c) order parameters of FM and stripy states, $|\langle\hat{\boldsymbol{S}}\rangle|_{\rm FM}$ and $|\langle\hat{\boldsymbol{S}}\rangle|_{\rm stripy}$, respectively. Two dashed lines are the phase boundaries of the three phases: $\phi/\pi \approx -0.645$ and $-0.625$. Here, we set $(D, \chi) = (8, 64)$.

#### 2. FM–FQ–stripy transition

In this subsubsection, we illustrate results of the FM–FQ–stripy transition by calculating some order parameters when tuning the parameter $\phi$ and fixing $\theta$ at $\theta = 0.9\pi$. We calculate the norms of the spin dipolar and quadrupolar moments, $|\langle\hat{\boldsymbol{S}}\rangle|$ and $|\langle\hat{\boldsymbol{Q}}\rangle|_{\rm FQ}$ respectively, to see magnetic orders [see Figs. 5(a) and 5(b)]. As shown in Fig. 5(a), $|\langle\hat{\boldsymbol{S}}\rangle|$ remains finite except for a narrow middle region where it suddenly drops to 0. Also, we confirm an increase of $|\langle\hat{\boldsymbol{Q}}\rangle|_{\rm FQ}$ in this narrow region [see Fig. 5(b)]. According to these results, we determine that this middle region is the FQ phase whose boundaries are $\phi/\pi \approx -0.645$ and $-0.625$.

Next, we define two order parameters to determine magnetic orders. We define an FM order parameter as

$$|\langle\hat{\boldsymbol{S}}\rangle|_{\rm FM} \equiv \sqrt{\sum_{\gamma=x,y,z} \langle\hat{S}^{\gamma}\rangle^2_{\rm FM}}, \tag{11}$$

$$\langle\hat{S}^{\gamma}\rangle_{\rm FM} \equiv \frac{1}{8}\sum_{i\in\{0,\cdots,7\}} \langle\hat{S}^{\gamma}_i\rangle. \tag{12}$$

Similarly, we write a stripy order parameter as $|\langle\hat{\boldsymbol{S}}\rangle|_{\rm stripy} \equiv \max\{|\langle\hat{\boldsymbol{S}}\rangle|_{\rm stripy1}, |\langle\hat{\boldsymbol{S}}\rangle|_{\rm stripy2}, |\langle\hat{\boldsymbol{S}}\rangle|_{\rm stripy3}\}$ and

$$|\langle\hat{\boldsymbol{S}}\rangle|_{{\rm stripy}a} \equiv \sqrt{\sum_{\gamma=x,y,z} \langle\hat{S}^{\gamma}\rangle^2_{{\rm stripy}a}}, \tag{13}$$

$$\langle\hat{S}^{\gamma}\rangle_{{\rm stripy}a} \equiv \frac{1}{8}\left(\sum_{i\in A_a} - \sum_{i\in B_a}\right)\langle\hat{S}^{\gamma}_i\rangle, \tag{14}$$

where $A_a$ and $B_a$ $(a = 1, 2, 3)$ are sets of sites in the unit cell Fig. 2, defined as $A_1 = \{0, 2, 4, 6\}$, $B_1 = \{1, 3, 5, 7\}$, $A_2 = \{0, 1, 4, 7\}$, $B_2 = \{2, 3, 5, 6\}$, $A_3 = \{0, 3, 4, 5\}$, $B_3 = \{1, 2, 6, 7\}$. Namely, $|\langle\hat{\boldsymbol{S}}\rangle|_{\rm stripy}$ becomes a finite value if spins take any stripy ordered configurations shown in Fig. 1(b), and 0 otherwise. From Fig. 5(c), we find that the left-hand side magnetic region is the FM phase, while the right-hand side one is the stripy phase. Note that the direct FM–stripy does not appear unlike Refs. [44,45] since the FQ phase get between them, which can only be detected by appropriately illustrating quantum entanglements ascribed for the ferro-Kitaev interaction utilizing the iPEPS.

### C. Vicinity of the antiferro-Kitaev limit

In this subsection, we explain how to detect phases by calculating order parameters with the emphasis on the vicinity of antiferro-Kitaev limit ($\theta = 0$). In later subsubsections, we show our numerical results in the cases of the AKSL–FQ and zigzag–FQ–AFM transitions.

#### 1. AKSL–FQ transition

In this subsection, we show our numerical results illustrating the AKSL–FQ transition, in the vicinity of the antiferro-Kitaev limit ($\theta = 0$). We show the physical quantities by varying the parameter $\theta$, while keeping $\phi$ fixed at arctan(2).

To begin with, we investigate dipolar and quadrupolar orders as shown in Figs. 6(a) and 6(b). Although $|\langle\hat{\boldsymbol{S}}\rangle|$ stays 0 in the whole range of $0 \leqslant \theta/\pi \leqslant 0.01$, we confirm that $|\langle\hat{\boldsymbol{Q}}\rangle|_{\rm FQ}$ shows a sharp jump at $\theta/\pi \approx 0.00285$. $|\langle\hat{\boldsymbol{Q}}\rangle|_{\rm FQ}$ becomes small but finite in the right-hand side area near the boundary $\theta/\pi \approx 0.00285$. However, we expect that this approaches to 0 if we increase the bond dimension $D$. We therefore determine the right-hand side region with the finite $|\langle\hat{\boldsymbol{Q}}\rangle|_{\rm FQ}$ is the FQ phase. We then examine the flux $\langle\hat{W}_p\rangle$ to see the vortex freeness. Figure 6(c) also shows a small jump of $\langle\hat{W}_p\rangle$ at the boundary $\theta/\pi = 0.00285$. From this result, we determine the left-hand side area $(0.0 \lesssim \theta/\pi \leqslant 0.00285)$ is the AKSL phase since $|\langle\hat{\boldsymbol{S}}\rangle| = |\langle\hat{\boldsymbol{Q}}\rangle|_{\rm FQ} \approx 0$ and $\langle\hat{W}_p\rangle \approx 1$. Interestingly, similar to the case near the antiferro-Kitaev limit, $\langle\hat{W}_p\rangle$ takes the value near to 1 even in the FQ phase, showing the vortex freeness of the FQ phase strongly influenced by the AKSL phase.

#### 2. Zigzag–FQ–AFM transition

In this subsection, we explain results of the zigzag–FQ–AFM transition by calculating some order parameters when tuning the parameter $\phi$ and fixing $\theta$ at $\theta = 0.01\pi$. We calculate $|\langle\hat{\boldsymbol{S}}\rangle|$ and $|\langle\hat{\boldsymbol{Q}}\rangle|_{\rm FQ}$ to see magnetic orders [see Figs. 7(a) and 7(b)]. As shown in Fig. 7(a), $|\langle\hat{\boldsymbol{S}}\rangle|$ remains finite values except for an intermediate extended region $-0.745 \leqslant \phi/\pi \leqslant -0.595$, where it suddenly drops to 0. We also confirm a sharp jump of $|\langle\hat{\boldsymbol{Q}}\rangle|_{\rm FQ}$ in this region [see Fig. 7(b)]. We thus determine that this intermediate region is the FQ phase.

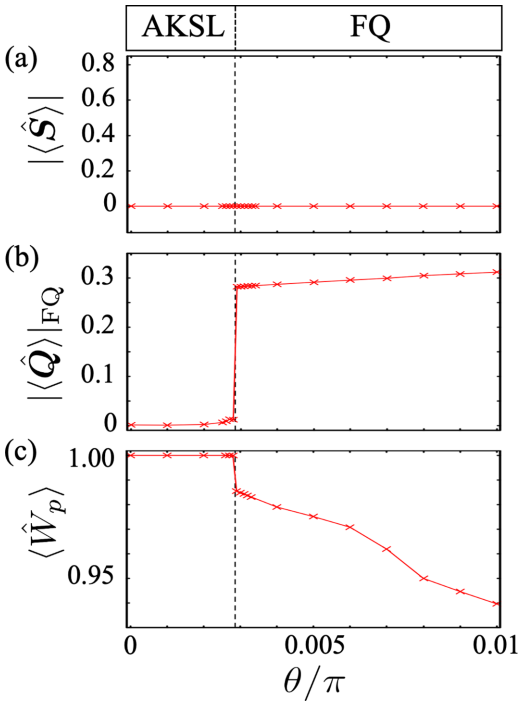


FIG. 6. Numerical results as a function of $\theta$ when fixing $\phi$ at $\phi = \arctan(2) \approx -0.648\pi$. (a) Norm of spin $|\langle\hat{\boldsymbol{S}}\rangle|$, (b) ferro-quadrupolar order parameter $|\langle\hat{\boldsymbol{Q}}\rangle|_{\rm FQ}$, (c) flux $\langle\hat{W}_p\rangle$. The dashed line is the phase boundary between AKSL phase and FQ phase: $\theta/\pi \approx 0.00285$. Here, we set $(D, \chi) = (8, 128)$.

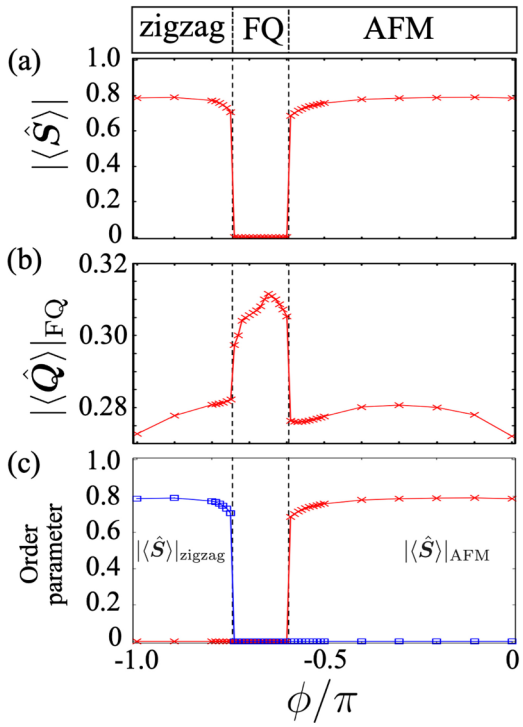


FIG. 7. Numerical results as a function of $\phi$ when fixing $\theta$ at $\theta = 0.01\pi$. (a) Norm of spin $|\langle\hat{\boldsymbol{S}}\rangle|$, (b) ferro-quadrupolar order parameter $|\langle\hat{\boldsymbol{Q}}\rangle|_{\rm FQ}$, (c) order parameters of zigzag and AFM states, $|\langle\hat{\boldsymbol{S}}\rangle|_{\rm zigzag}$ and $|\langle\hat{\boldsymbol{S}}\rangle|_{\rm AFM}$, respectively. Two dashed lines are the phase boundaries of the three phases: $\phi/\pi \approx -0.745$ and $-0.595$. Here, we set $(D, \chi) = (8, 64)$.

Next, we derive two order parameters to determine what phases the magnetic ordered regions are. We defined an AFM order parameter as

$$|\langle\hat{\boldsymbol{S}}\rangle|_{\rm AFM} \equiv \sqrt{\sum_{\gamma=x,y,z} \langle\hat{S}^{\gamma}\rangle^2_{\rm AFM}}, \tag{15}$$

$$\langle\hat{S}^{\gamma}\rangle_{\rm AFM} \equiv \frac{1}{8}\left(\sum_{i\in\{0,2,5,7\}} - \sum_{i\in\{1,3,4,6\}}\right)\langle\hat{S}^{\gamma}_i\rangle. \tag{16}$$

Also, we defined a zigzag order parameter as $|\langle\hat{\boldsymbol{S}}\rangle|_{\rm zigzag} \equiv \max\{|\langle\hat{\boldsymbol{S}}\rangle|_{\rm zigzag1}, |\langle\hat{\boldsymbol{S}}\rangle|_{\rm zigzag2}, |\langle\hat{\boldsymbol{S}}\rangle|_{\rm zigzag3}\}$ and

$$|\langle\hat{\boldsymbol{S}}\rangle|_{{\rm zigzag}a} \equiv \sqrt{\sum_{\gamma=x,y,z} \langle\hat{S}^{\gamma}\rangle^2_{{\rm zigzag}a}}, \tag{17}$$

$$\langle\hat{S}^{\gamma}\rangle_{{\rm zigzag}a} \equiv \frac{1}{8}\left(\sum_{i\in C_a} - \sum_{i\in D_a}\right)\langle\hat{S}^{\gamma}_i\rangle, \tag{18}$$

where $C_a$ and $D_a$ $(a = 1, 2, 3)$ are sets of sites in the unit cell Fig. 2, defined as $C_1 = \{0, 1, 2, 3\}$, $D_1 = \{4, 5, 6, 7\}$, $C_2 = \{0, 3, 6, 7\}$, $D_2 = \{1, 2, 4, 5\}$, $C_3 = \{0, 1, 5, 6\}$, $D_3 = \{2, 3, 4, 7\}$. Namely, $|\langle\hat{\boldsymbol{S}}\rangle|_{\rm zigzag}$ becomes a finite value if spins take any zigzag ordered configurations shown in Fig. 1(b), and 0 otherwise. From Fig. 7(c), we find that the left-hand side magnetic region is the zigzag phase, while the right-hand side one is the AFM phase. Unlike Refs. [44,45], according to Figs. 3(c) and 7, the direct zigzag–AFM does not occur since the FQ phase enters between them, which can only be discovered by appropriately illustrating quantum entanglement by iPEPS.

## V. CONCLUSIONS AND DISCUSSION

In order to probe quantum phases and phase transitions ascribed for the competition between the KSL and the spin-nematic states, we numerically investigate the BBQ-K model Eq. (1), which was originally proposed in Refs. [44,45]. Utilizing the 2D iPEPS, we take into account quantum entanglements among spins ignored in Refs. [44,45]. Then, we could represent quantum properties of the KSL more precisely. As a result, we succeed in constructing the phase diagram [see Figs. 1(a) and 3], including extended KSL phases, which could not, in principle, be captured by the semiclassical variational calculations in Refs. [44,45]. More specifically, we result in discovering several properties: (1) We detect the direct KSL-FQ phase transitions (see Fig. 3). (2) The FKSL phase is stabilized under the almost pure ferro-quadrupolar perturbation [see Fig. 3(a)]. (3) The FQ phase is more robust against the Heisenberg interaction than one obtained in Refs. [44,45], and it gets extended when the antiferro-Kitaev interaction becomes dominant [see Fig. 3(b)]. Note that, as far as we know, a direct phase transition between a quantum spin liquid phase and the FQ phase is discovered in higher spin-$S$ systems, although similar results were obtained [73] in the spin-1/2 system as for a bond-nematic state.

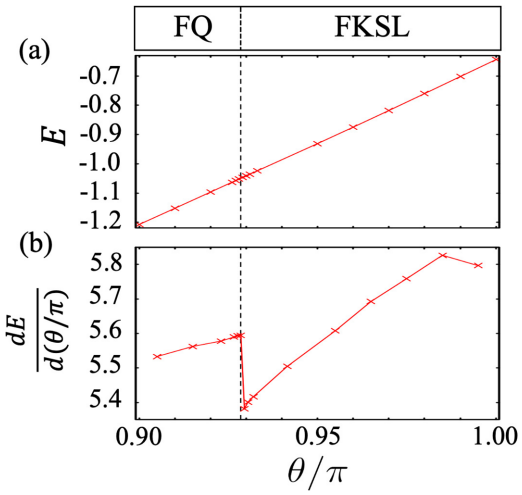


FIG. 8. Numerical results as a function of $\theta$ when fixing $\phi$ at $\phi = -0.63\pi$. (a) Energy $E$ and (b) first derivative of the energy. Here, we set $(D, \chi) = (8, 128)$.

As an open problem, we could not determine whether the phase transitions seen in this paper are the second-ordered or first-ordered transition. As shown in Fig. 8, we calculate the energy and its first derivative to determine the order of the phase transitions. As for the first derivative, we consider the numerical differentiation as

$$\left.\frac{dE}{d\theta}\right|_{\theta=\theta'-\frac{\Delta\theta}{2}} \approx \frac{E(\theta') - E(\theta' - \Delta\theta)}{\Delta\theta}, \tag{19}$$

based on the numerical data at $\theta'$ and $\theta' - \Delta\theta$. We here confirm that the first derivative shows a jump describing the first-ordered transition in the case of $\phi = -0.63\pi$ near the ferro-Kitaev limit [see Fig. 8(b)]. Similar results were obtained in the other cases listed in Sec. IV. However, these results seem to be not reliable. The ITE utilizing the simple update could not appropriately capture the long-range correlation, and thus, the ground states obtained by iPEPS strongly depend on initial states. Therefore, we could not rule out the possibility of the second-ordered transition.

Another open problem is the nature of the phase diagram for the positive quadrupolar interaction $J_2 > 0$ ($0 \leqslant \phi \leqslant \pi$), where Refs. [44,45] proposed several exotic phases. In this region, the AFQ order appeared in classical spin-1 systems [50,51] is melted by strong quantum fluctuation emerged from the competition between the Heisenberg and the positive biquadratic (quadrupolar) terms. Instead, there appears [49,52] plaquette valence-bond solid state characterized by the plaquette order breaking translational symmetry. Investigating the interplay between the KSL and the positive quadrupolar interaction seems to be an interesting near future task, which may require more computational cost than the case of this paper, namely $D \geqslant 9$, according to the numerical study with the SU(3) Heisenberg model [52]. Since the positive quadrupolar interaction is expected in materials with orbital degeneracy [74–76], investigating the models with $J_2 > 0$ might be relevant for understanding the nature of these materials.

One of future tasks is an investigation of the low-energy excitation, which offer clear guidelines for experiments with inelastic neutron scattering. This excitation is expected to be

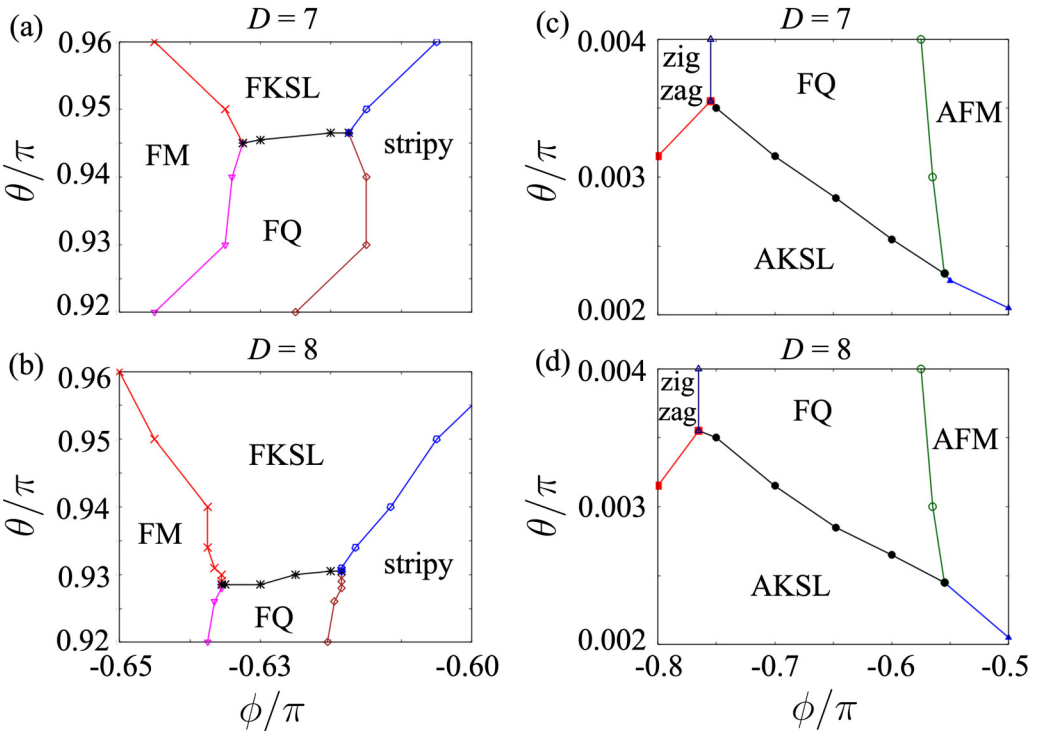


FIG. 9. Phase diagrams in the vicinity of ferro-Kitaev limit ($\theta = \pi$) with (a) $D = 7$ and (b) $D = 8$, and in the vicinity of antiferro-Kitaev limit ($\theta = 0$) with (c) $D = 7$ and (d) $D = 8$. We set the bond dimension $\chi = D^2$ or $2D^2$, where we adopt $\chi = 2D^2$ if the CTMRG does not converge in the case of $\chi = D^2$.

caused by waves of local order parameters in the BBQ-K model. For describing this excitation, one should utilize the SU(3) flavor-wave theory [41,77,78], since the conventional SU(2) spin-wave theory fails to illustrate quadrupolar fluctuations ascribed for the biquadratic term [79–83].

Finally, we discuss implications of our results for experiments. According to our numerical results in Fig. 3(a), the FKSL phase can realize even with a relatively weak ferro-Kitaev interaction, if the pure ferro-quadrupolar interaction exists. Therefore, our phase diagrams and results in Sec. IV B offer clues for experiments searching for materials showing FKSL state. On the other hand, the AKSL phase is vulnerable to the ferro-quadrupolar interaction [see Fig. 3(b)], unlike the FKSL phase. This result may offer clues for experiments with candidate antiferro-Kitaev materials like $A_3Ni_2XO_6$ ($A$ = Li, Na, $X$ = Bi, Sb) [35] to detect the AKSL–FQ transition. We desire that our results will stimulate further experimental and theoretical studies on the interplay between the KSL and the spin nematic states.

## ACKNOWLEDGMENTS

We appreciate R. Pohle and Y. Motome for helpful discussions. Our work was financially supported by Japan Society for the Promotion of Science KAKENHI, Grants No. 20H00122, No. 22H01179, No. 23H03818, No. 22K18682, and by the Center of Innovations for Sustainable Quantum AI (JST Grant No. JPMJPF2221). T.O. acknowledges the support from the Endowed Project for Quantum Software Research and Education, The University of Tokyo. We utilized the tensor-network software, named TeNeS [71,72] for iPEPS calculations. Our numerical calculations was implemented by the Supercomputer Center of the Institute for Solid State Physics, the University of Tokyo.

## APPENDIX: DEPENDENCY ON THE BOND DIMENSION $D$

In this section, we describe the $D$ dependency of the phase boundaries. Figure 9 shows the phase diagrams in the vicinity of two Kitaev limits with $D = 7$ and 8. Also, Fig. 10 denotes the ferro-quadrupolar order parameter $|\langle\hat{\boldsymbol{Q}}\rangle|_{\mathrm{FQ}}$ with several bond dimensions in the vicinity of the Kitaev limits to detect phase boundaries. We set the bond dimension $\chi = D^2$ or $2D^2$, where we adopt $\chi = 2D^2$ if the CTMRG does not converge in the case of $\chi = D^2$.

As for the vicinity of the ferro-Kitaev limit ($\theta = \pi$), the FKSL phase gets broader as the bond dimension $D$ increases [see Figs. 9(a) and 9(b), and Fig. 10(a)]. According to these results, we could more efficiently capture the robustness of the FKSL phase against the ferro-quadrupolar interaction, as the bond dimension $D$ increases. But we could not determine the phase boundary with $D = 9$ since the CTMRG does not converge in the vicinity of the boundary even with $\chi = 2D^2$. There remains the possibility that the FKSL phase gets more robust if $D \geqslant 9$, that is, determining the FKSL–FQ phase boundary is open to discussion. Despite these difficulties, we confirm that these results do not matter our conclusions of "direct FQ–FKSL transition" and "robustness of the FKSL phase"

On the other hand, regarding the vicinity of the antiferro-Kitaev limit ($\theta = 0$), the phase diagrams do not change so much even when the bond dimension $D$ increases [see Figs. 9(c) and 9(d)]. As shown in Fig. 10(b), the FQ–AKSL phase boundary is almost invariant if $D \geqslant 7$. Therefore, our results with $D = 8$ in Sec. IV seem to converge sufficiently in the vicinity of the antiferro-Kitaev limit, which supports our conclusions of "direct AKSL–FQ transition" and "extension of the FQ phase".

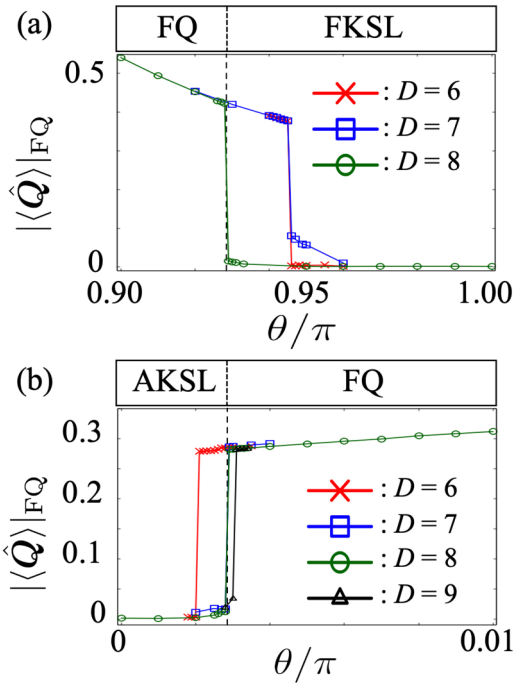


FIG. 10. Ferro-quadrupolar order parameter $|\langle\hat{\boldsymbol{Q}}\rangle|_{\mathrm{FQ}}$ with several bond dimension $D$ in the vicinity of (a) ferro-Kitaev limit ($\theta = \pi$) and $\phi = -0.63\pi$, and (b) antiferro-Kitaev limit ($\theta = 0$) and $\phi = \arctan(2) \approx -0.648\pi$. The dashed lines in these figures are phase boundaries in the case of $D = 8$ in Sec. IV.

[1] A. Kitaev, Anyons in an exactly solved model and beyond, Ann. Phys. (NY) **321**, 2 (2006).

[2] G. Jackeli and G. Khaliullin, Mott insulators in the strong spin-orbit coupling limit: From Heisenberg to a quantum compass and Kitaev models, Phys. Rev. Lett. **102**, 017205 (2009).

[3] Y. Kasahara, T. Ohnishi, Y. Mizukami, O. Tanaka, S. Ma, K. Sugii, N. Kurita, H. Tanaka, J. Nasu, Y. Motome *et al.*, Majorana quantization and half-integer thermal quantum Hall effect in a Kitaev spin liquid, Nature (London) **559**, 227 (2018).

[4] K. W. Plumb, J. P. Clancy, L. J. Sandilands, V. V. Shankar, Y. F. Hu, K. S. Burch, H.-Y. Kee, and Y.-J. Kim, $\alpha$-$RuCl_3$: A spin-orbit assisted Mott insulator on a honeycomb lattice, Phys. Rev. B **90**, 041112(R) (2014).

[5] A. Banerjee, C. A. Bridges, J. Q. Yan, A. A. Aczel, L. Li, M. B. Stone, G. E. Granroth, M. D. Lumsden, Y. Yiu, J. Knolle *et al.*, Proximate Kitaev quantum spin liquid behaviour in a honeycomb magnet, Nat. Mater. **15**, 733 (2016).

[6] S. M. Winter, K. Riedl, P. A. Maksimov, A. L. Chernyshev, A. Honecker, and R. Valentí, Breakdown of magnons in a strongly spin-orbital coupled magnet, Nat. Commun. **8**, 1152 (2017).

[7] A. Little, L. Wu, P. Lampen-Kelley, A. Banerjee, S. Patankar, D. Rees, C. A. Bridges, J.-Q. Yan, D. Mandrus, S. E. Nagler, and J. Orenstein, Antiferromagnetic resonance and terahertz continuum in $\alpha$-$RuCl_3$, Phys. Rev. Lett. **119**, 227201 (2017).

[8] Z. Wang, S. Reschke, D. Hüvonen, S.-H. Do, K.-Y. Choi, M. Gensch, U. Nagel, T. Rõõm, and A. Loidl, Magnetic excitations and continuum of a possibly field-induced quantum spin liquid in $\alpha$-$RuCl_3$, Phys. Rev. Lett. **119**, 227202 (2017).

[9] K. Ran, J. Wang, W. Wang, Z.-Y. Dong, X. Ren, S. Bao, S. Li, Z. Ma, Y. Gan, Y. Zhang, J. T. Park, G. Deng, S. Danilkin, S.-L. Yu, J.-X. Li, and J. Wen, Spin-wave excitations evidencing the Kitaev interaction in single crystalline $\alpha$-$RuCl_3$, Phys. Rev. Lett. **118**, 107203 (2017).

[10] J. Chaloupka, G. Jackeli, and G. Khaliullin, Kitaev-Heisenberg model on a honeycomb lattice: Possible exotic phases in iridium oxides $A_2IrO_3$, Phys. Rev. Lett. **105**, 027204 (2010).

[11] J. Chaloupka, G. Jackeli, and G. Khaliullin, Zigzag magnetic order in the iridium oxide $Na_2IrO_3$, Phys. Rev. Lett. **110**, 097204 (2013).

[12] S. H. Chun, J.-W. Kim, J. Kim, H. Zheng, C. C. Stoumpos, C. D. Malliakas, J. F. Mitchell, K. Mehlawat, Y. Singh, Y. Choi *et al.*, Direct evidence for dominant bond-directional interactions in a honeycomb lattice iridate $Na_2IrO_3$, Nat. Phys. **11**, 462 (2015).

[13] S. K. Choi, R. Coldea, A. N. Kolmogorov, T. Lancaster, I. I. Mazin, S. J. Blundell, P. G. Radaelli, Y. Singh, P. Gegenwart, K. R. Choi, S.-W. Cheong, P. J. Baker, C. Stock, and J. Taylor, Spin waves and revised crystal structure of honeycomb iridate $Na_2IrO_3$, Phys. Rev. Lett. **108**, 127204 (2012).

[14] Y. Singh and P. Gegenwart, Antiferromagnetic Mott insulating state in single crystals of the honeycomb lattice material $Na_2IrO_3$, Phys. Rev. B **82**, 064412 (2010).

[15] Y. Singh, S. Manni, J. Reuther, T. Berlijn, R. Thomale, W. Ku, S. Trebst, and P. Gegenwart, Relevance of the Heisenberg-Kitaev model for the honeycomb lattice iridates $A_2IrO_3$, Phys. Rev. Lett. **108**, 127203 (2012).

[16] V. M. Katukuri, S. Nishimoto, V. Yushankhai, A. Stoyanova, H. Kandpal, S. Choi, R. Coldea, I. Rousochatzakis, L. Hozoi, and J. van den Brink, Kitaev interactions between $j = 1/2$ moments in honeycomb $Na_2IrO_3$ are large and ferromagnetic: Insights from *ab initio* quantum chemistry calculations, New J. Phys. **16**, 013056 (2014).

[17] S. C. Williams, R. D. Johnson, F. Freund, S. Choi, A. Jesche, I. Kimchi, S. Manni, A. Bombardi, P. Manuel, P. Gegenwart, and R. Coldea, Incommensurate counterrotating magnetic order stabilized by Kitaev interactions in the layered honeycomb $\alpha$-$Li_2IrO_3$, Phys. Rev. B **93**, 195158 (2016).

[18] J. G. Rau, E. Kin-Ho Lee, and H.-Y. Kee, Generic spin model for the honeycomb iridates beyond the Kitaev limit, Phys. Rev. Lett. **112**, 077204 (2014).

[19] S. Bette, T. Takayama, K. Kitagawa, R. Takano, H. Takagi, and R. E. Dinnebier, Solution of the heavily stacking faulted crystal structure of the honeycomb iridate $H_3LiIr_2O_6$, Dalton Trans. **46**, 15216 (2017).

[20] I. Kimchi and Y.-Z. You, Kitaev-Heisenberg-$J_2$-$J_3$ model for the iridates $A_2IrO_3$, Phys. Rev. B **84**, 180407(R) (2011).

[21] J. Nasu, M. Udagawa, and Y. Motome, Vaporization of Kitaev spin liquids, Phys. Rev. Lett. **113**, 197205 (2014).

[22] J. Yoshitake, J. Nasu, and Y. Motome, Fractional spin fluctuations as a precursor of quantum spin liquids: Majorana dynamical mean-field study for the Kitaev model, Phys. Rev. Lett. **117**, 157203 (2016).

[23] A. Catuneanu, Y. Yamaji, G. Wachtel, Y. B. Kim, and H.-Y. Kee, Path to stable quantum spin liquids in spin-orbit coupled correlated materials, npj Quantum Mater. **3**, 23 (2018).

[24] M. Gohlke, G. Wachtel, Y. Yamaji, F. Pollmann, and Y. B. Kim, Quantum spin liquid signatures in Kitaev-like frustrated magnets, Phys. Rev. B **97**, 075126 (2018).

[25] H.-Y. Lee, R. Kaneko, T. Okubo, and N. Kawashima, Gapless Kitaev spin liquid to classical string gas through tensor networks, Phys. Rev. Lett. **123**, 087203 (2019).

[26] H.-Y. Lee, R. Kaneko, L. E. Chern, T. Okubo, Y. Yamaji, N. Kawashima, and Y. B. Kim, Magnetic field induced quantum phases in a tensor network study of Kitaev magnets, Nat. Commun. **11**, 1639 (2020).

[27] S.-S. Zhang, G. B. Halász, and C. D. Batista, Theory of the Kitaev model in a [111] magnetic field, Nat. Commun. **13**, 399 (2022).

[28] G. Baskaran, D. Sen, and R. Shankar, Spin-$S$ Kitaev model: Classical ground states, order from disorder, and exact correlation functions, Phys. Rev. B **78**, 115116 (2008).

[29] J. Oitmaa, A. Koga, and R. R. P. Singh, Incipient and well-developed entropy plateaus in spin-$S$ Kitaev models, Phys. Rev. B **98**, 214404 (2018).

[30] A. Koga, H. Tomishige, and J. Nasu, Ground-state and thermodynamic properties of an $S = 1$ Kitaev model, J. Phys. Soc. Jpn. **87**, 063703 (2018).

[31] H.-Y. Lee, N. Kawashima, and Y. B. Kim, Tensor network wave function of $S = 1$ Kitaev spin liquids, Phys. Rev. Res. **2**, 033318 (2020).

[32] X.-Y. Dong and D. N. Sheng, Spin-1 Kitaev-Heisenberg model on a honeycomb lattice, Phys. Rev. B **102**, 121102(R) (2020).

[33] I. Khait, P. P. Stavropoulos, H.-Y. Kee, and Y. B. Kim, Characterizing spin-one Kitaev quantum spin liquids, Phys. Rev. Res. **3**, 013160 (2021).

[34] Z. Zhu, Z.-Y. Weng, and D. N. Sheng, Magnetic field induced spin liquids in $S = 1$ Kitaev honeycomb model, Phys. Rev. Res. **2**, 022047(R) (2020).

[35] P. P. Stavropoulos, D. Pereira, and H.-Y. Kee, Microscopic mechanism for a higher-spin Kitaev model, Phys. Rev. Lett. **123**, 037203 (2019).

[36] I. Lee, F. G. Utermohlen, D. Weber, K. Hwang, C. Zhang, J. van Tol, J. E. Goldberger, N. Trivedi, and P. C. Hammel, Fundamental spin interactions underlying the magnetic anisotropy in the Kitaev ferromagnet $CrI_3$, Phys. Rev. Lett. **124**, 017201 (2020).

[37] C. Xu, J. Feng, M. Kawamura, Y. Yamaji, Y. Nahas, S. Prokhorenko, Y. Qi, H. Xiang, and L. Bellaiche, Possible Kitaev quantum spin liquid state in 2D materials with $S = 3/2$, Phys. Rev. Lett. **124**, 087205 (2020).

[38] M. Blume and Y. Y. Hsieh, Biquadratic exchange and quadrupolar ordering, J. Appl. Phys. **40**, 1249 (1969).

[39] V. M. Matveev, Quantum quadrupolar magnetism and phase transitions in the presence of biquadratic exchange, Sov. Phys. JETP **38**, 813 (1974).
[40] H. Tsunetsugu and M. Arikawa, Spin nematic phase in $S = 1$ triangular antiferromagnets, J. Phys. Soc. Jpn. **75**, 083701 (2006).
[41] A. Läuchli, F. Mila, and K. Penc, Quadrupolar phases of the $S = 1$ bilinear-biquadratic Heisenberg model on the triangular lattice, Phys. Rev. Lett. **97**, 087205 (2006).
[42] K. Penc and A. M. Läuchli, Spin nematic phases in quantum spin systems, in *Introduction to Frustrated Magnetism: Materials, Experiments, Theory*, edited by C. Lacroix, P. Mendels, and F. Mila (Springer, Berlin, 2011), pp. 331–362.
[43] C. Lacroix, P. Mendels, and F. Mila, Introduction to quantum spin liquids, in *Introduction to Frustrated Magnetism: Materials, Experiments, Theory*, edited by C. Lacroix, P. Mendels, and F. Mila (Springer, Berlin, 2011), pp. 23–41
[44] R. Pohle, N. Shannon, and Y. Motome, Spin nematics meet spin liquids: Exotic quantum phases in the spin-1 bilinear-biquadratic model with Kitaev interactions, Phys. Rev. B **107**, L140403 (2023).
[45] R. Pohle, N. Shannon, and Y. Motome, Eight-color chiral spin liquid in the $S = 1$ bilinear-biquadratic model with Kitaev interactions, Phys. Rev. Res. **6**, 033077 (2024).
[46] F. Verstraete and J. I. Cirac, Renormalization algorithms for quantum-many body systems in two and higher dimensions, arXiv:cond-mat/0407066.
[47] F. Verstraete and J. I. Cirac, Valence-bond states for quantum computation, Phys. Rev. A **70**, 060302(R) (2004).
[48] J. Jordan, R. Orús, G. Vidal, F. Verstraete, and J. I. Cirac, Classical simulation of infinite-size quantum lattice systems in two spatial dimensions, Phys. Rev. Lett. **101**, 250602 (2008).
[49] H. H. Zhao, C. Xu, Q. N. Chen, Z. C. Wei, M. P. Qin, G. M. Zhang, and T. Xiang, Plaquette order and deconfined quantum critical point in the spin-1 bilinear-biquadratic Heisenberg model on the honeycomb lattice, Phys. Rev. B **85**, 134416 (2012).
[50] H. H. Chen and P. M. Levy, Dipole and quadrupole phase transitions in spin-1 models, Phys. Rev. B **7**, 4267 (1973).
[51] N. Papanicolaou, Unusual phases in quantum spin-1 systems, Nucl. Phys. B **305**, 367 (1988).
[52] P. Corboz, M. Lajkó, K. Penc, F. Mila, and A. M. Läuchli, Competing states in the SU(3) Heisenberg model on the honeycomb lattice: Plaquette valence-bond crystal versus dimerized color-ordered state, Phys. Rev. B **87**, 195113 (2013).
[53] T. Nishino, Y. Hieida, K. Okunishi, N. Maeshima, Y. Akutsu, and A. Gendiar, Two-dimensional tensor product variational formulation, Prog. Theor. Phys. **105**, 409 (2001).
[54] F. Verstraete, V. Murg, and J. I. Cirac, Matrix product states, projected entangled pair states, and variational renormalization group methods for quantum spin systems, Adv. Phys. **57**, 143 (2008).
[55] M. Srednicki, Entropy and area, Phys. Rev. Lett. **71**, 666 (1993).
[56] T. Xiang, J. Lou, and Z. Su, Two-dimensional algorithm of the density-matrix renormalization group, Phys. Rev. B **64**, 104414 (2001).
[57] P. Calabrese and J. Cardy, Entanglement entropy and quantum field theory, J. Stat. Mech. (2004) P06002.
[58] R. Orús, A practical introduction to tensor networks: Matrix product states and projected entangled pair states, Ann. Phys. (NY) **349**, 117 (2014).
[59] H. F. Trotter, On the product of semi-groups of operators, Proc. Amr. Math. Soc. **10**, 545 (1959).
[60] M. Suzuki, Pair-product model of Heisenberg ferromagnets, J. Phys. Soc. Jpn. **21**, 2274 (1966).
[61] M. Suzuki, Relationship between $d$-dimensional quantal spin systems and $(d+1)$-dimensional Ising systems: Equivalence, critical exponents and systematic approximants of the partition function and spin correlations, Prog. Theor. Phys. **56**, 1454 (1976).
[62] G. Vidal, Efficient classical simulation of slightly entangled quantum computations, Phys. Rev. Lett. **91**, 147902 (2003).
[63] H. C. Jiang, Z. Y. Weng, and T. Xiang, Accurate determination of tensor network state of quantum lattice models in two dimensions, Phys. Rev. Lett. **101**, 090603 (2008).
[64] R. J. Baxter, Dimers on a rectangular lattice, J. Math. Phys. **9**, 650 (1968).
[65] R. J. Baxter, Variational approximations for square lattice models in statistical mechanics, J. Stat. Phys. **19**, 461 (1978).
[66] T. Nishino and K. Okunishi, Corner transfer matrix renormalization group method, J. Phys. Soc. Jpn. **65**, 891 (1996).
[67] R. Orús and G. Vidal, Simulation of two-dimensional quantum systems on an infinite lattice revisited: Corner transfer matrix for tensor contraction, Phys. Rev. B **80**, 094403 (2009).
[68] H. N. Phien, J. A. Bengua, H. D. Tuan, P. Corboz, and R. Orús, Infinite projected entangled pair states algorithm improved: Fast full update and gauge fixing, Phys. Rev. B **92**, 035142 (2015).
[69] C.-Y. Lee, B. Normand, and Y.-J. Kao, Gapless spin liquid in the kagome Heisenberg antiferromagnet with Dzyaloshinskii-Moriya interactions, Phys. Rev. B **98**, 224414 (2018).
[70] P. Corboz, T. M. Rice, and M. Troyer, Competing states in the $t$-$J$ model: Uniform $d$-wave state versus stripe state, Phys. Rev. Lett. **113**, 046402 (2014).
[71] Y. Motoyama, T. Okubo, K. Yoshimi, S. Morita, T. Kato, and N. Kawashima, TeNeS: Tensor network solver for quantum lattice systems, Comput. Phys. Commun. **279**, 108437 (2022).
[72] TeNeS, https://github.com/issp-center-dev/TeNeS.
[73] J. Nasu, Y. Kato, J. Yoshitake, Y. Kamiya, and Y. Motome, Spin-liquid–to–spin-liquid transition in Kitaev magnets driven by fractionalization, Phys. Rev. Lett. **118**, 137203 (2017).
[74] A. Yoshimori and S. Inagaki, Fourth order interaction effects on the antiferromagnetic structures. II. A phenomenological model for $NiS_2$, J. Phys. Soc. Jpn. **50**, 769 (1981).
[75] M. Hoffmann and S. Blügel, Systematic derivation of realistic spin models for beyond-Heisenberg solids, Phys. Rev. B **101**, 024418 (2020).
[76] R. Soni, N. Kaushal, C. Şen, F. A. Reboredo, A. Moreo, and E. Dagotto, Estimation of biquadratic and bicubic Heisenberg effective couplings from multiorbital Hubbard models, New J. Phys. **24**, 073014 (2022).
[77] N. Papanicolaou, Pseudospin approach for planar ferromagnets, Nucl. Phys. B **240**, 281 (1984).
[78] A. Joshi, M. Ma, F. Mila, D. N. Shi, and F. C. Zhang, Elementary excitations in magnetically ordered systems with orbital degeneracy, Phys. Rev. B **60**, 6584 (1999).
[79] A. L. Wysocki, K. D. Belashchenko, and V. P. Antropov, Consistent model of magnetism in ferropnictides, Nat. Phys. **7**, 485 (2011).

[80] D. Stanek, O. P. Sushkov, and G. S. Uhrig, Self-consistent spin-wave theory for a frustrated Heisenberg model with biquadratic exchange in the columnar phase and its application to iron pnictides, Phys. Rev. B **84**, 064505 (2011).

[81] J. Hu, B. Xu, W. Liu, N.-N. Hao, and Y. Wang, Unified minimum effective model of magnetic properties of iron-based superconductors, Phys. Rev. B **85**, 144403 (2012).

[82] R. Yu, Z. Wang, P. Goswami, A. H. Nevidomskyy, Q. Si, and E. Abrahams, Spin dynamics of a $J_1$-$J_2$-$k$ model for the paramagnetic phase of iron pnictides, Phys. Rev. B **86**, 085148 (2012).

[83] P. Bilbao Ergueta and A. H. Nevidomskyy, Ising-nematic order in the bilinear-biquadratic model for the iron pnictides, Phys. Rev. B **92**, 165102 (2015).